Continental Shelf Research 91 (2014) 232–246

Contents lists available at ScienceDirect

Continental Shelf Research

journal homepage: www.elsevier.com/locate/csr

Spatial patterns of warming off Western Australia during the 2011 Ningaloo Niño: Quantifying impacts of remote and local forcing

Jessica Benthuysen [a,b], Ming Feng [c,*], Liejun Zhong [c]

[a] Institute for Marine and Antarctic Studies, University of Tasmania, Hobart, Tasmania, Australia
[b] ARC Centre of Excellence for Climate System Science, University of Tasmania, Hobart, Tasmania, Australia
[c] CSIRO Oceans and Atmosphere Flagship, Floreat, Western Australia, Australia

ARTICLE INFO

Article history:
Received 24 April 2014
Received in revised form
18 August 2014
Accepted 22 September 2014
Available online 22 October 2014

Keywords:
Eastern boundary currents
Leeuwin Current
Marine heat wave
La Niña

ABSTRACT

In austral summer 2011, an unprecedented Ningaloo Niño event occurred off the west coast of Australia, with sea surface temperature anomalies reaching 5 °C and significant impacts on marine ecosystems. In this study, a high resolution (~2 km) hydrodynamic model (Regional Ocean Modeling System) is used to simulate the variations in the near-surface temperature in the region from 2009 through mid-2011. Model results indicate that the peak temperatures in the broad mid-west coast of Australia during the event are predominantly due to poleward advection of warmer, tropical water (≈2/3 contribution). In addition, positive air–sea heat flux into the ocean also contributes (≈1/3 contribution) to the rise in temperature. The anomalous advection of warm water is caused by changes in the poleward flowing Leeuwin Current due to both local and remote wind forcing. In early 2011, the Leeuwin Current intensified owing to remote forcing by the equatorial easterly wind anomalies in the Pacific Ocean associated with the 2010–2011 La Niña. In addition, the southerly winds off the west coast of Australia weakened, allowing the Leeuwin Current to further intensify in speed at the peak of the event. Concurrently, the inshore, equatorward Capes Current was suppressed and reversed direction. The poleward flow over the shelf contributed to near-shore warming in contrast to cooling by upwelling and equatorward advection from the Capes Current in previous years.

1. Introduction

In the austral summer of 2011, a Ningaloo Niño event occurred in which a marine heat wave led to extreme warming of Western Australia's coastal waters. The sea surface temperature (SST) was warmer by +2.5 °C than typical based on satellite records for a broad region of 400 km by 300 km off the coast (Feng et al., 2013). These SST anomalies were unprecedented in historical record of in-situ observations over 140 years (Pearce and Feng, 2013; Wernberg et al., 2013) and in coral proxy records over more than 200 years (Zinke et al., 2014). The coastal marine ecosystems were impacted by this warming, including damages to seagrass, invertebrates, and fish populations (Wernberg et al., 2013). Understanding the mechanisms responsible for the anomalous warming is important for predicting future marine heat wave impacts on fisheries and coastal ecosystems.

Off Western Australia, the poleward flowing Leeuwin Current (LC) is the dominant boundary current over the continental shelf, which brings warm, low-salinity water southward (Cresswell and Golding, 1980). Large meanders and mesoscale eddies develop from the LC as it flows southward along the coast (Feng et al., 2005, 2007; Meuleners et al., 2007; Paterson et al., 2008; Weller et al., 2011). Inshore of the LC, the wind-driven Capes Current (CC) emerges in austral summer. The CC carries cool water equatorward from Cape Leeuwin to as far north as Shark Bay (26 °S; Pearce and Pattiaratchi, 1999; Woo et al., 2006) and is associated with episodic upwelling along the coast (Rossi et al., 2013a,b). During February 2011, record-strength LC speeds were recorded and the LC volume transport of 8 Sv far exceeded 2 Sv from climatology or 5 Sv in typical winter conditions (Feng et al., 2013). The LC's intensification coincided with the peak of the strong 2010–2011 La Niña in the Pacific Ocean.

1.1. Remote forcing

On interannual timescales, the Leeuwin Current transport is influenced by the El Niño Southern Oscillation (Feng et al., 2003). During La Niña periods, easterly wind stress anomalies in the equatorial Pacific deepen the thermocline in the warm pool, generating positive sea level anomalies in the Western Pacific. This deep, warm water passes into the Indian Ocean and the associated positive sea level anomalies propagate down the west coast of Australia, contributing to the LC's intensification during La

* Corresponding author.
E-mail address: ming.feng@csiro.au (M. Feng).

http://dx.doi.org/10.1016/j.csr.2014.09.014

Niña (Feng et al., 2003). During the 2010–2011 La Niña, the easterly wind stress anomalies in the equatorial Pacific, 0.34 N m^{-2}, and the sea level anomalies off Fremantle (32°S), 0.3 m, were significantly larger than climatological averages from 1982 to 2011 (Feng et al., 2013).

1.2. Local forcing

Local wind forcing amplified the strengthening of the Leeuwin Current in austral summer 2011, which has inspired the name of Ningaloo Niño to refer to the possible local air–sea coupling (Feng et al., 2013; Kataoka et al., 2013). In addition to remote forcing, local wind and air–sea heat fluxes played a role in the 2011 warming event. Southerly winds over the shelf oppose the poleward LC and are strongest in austral summer (Feng et al., 2003). During January and February 2011, the southerly winds weakened in connection with an offshore negative sea level pressure anomaly (Feng et al., 2013). Thus, the local wind anomalies also contributed to accelerating the LC poleward (Feng et al., 2013). Reduced southerly winds led to changes in the air–sea heat flux, with heat flux products indicating a net heat flux into the ocean (Feng et al., 2013). Furthermore, an Argo float indicates that the warming was mostly trapped within the surface mixed layer, ranging from 40 m to 60 m depth, during the peak of the marine heat wave (Feng et al., 2013).

1.3. Present research

This work aims to determine the relative impacts of remote and local forcing in the warming off Western Australia during the 2011 Ningaloo Niño event. A high resolution numerical model is used to quantify the roles of temperature advection and heat flux via turbulent diffusion that resulted in the anomalous peak in temperature. The relationships between the forcings and the LC transport are investigated, since both local and remote wind forcing tend to accelerate the LC transport poleward (Feng et al., 2013; Pearce and Feng, 2013). We also examine the near-shore CC during this time period, as the intensification of the LC and associated onshore flows suppress upwelling (e.g. Rossi et al., 2013b) and the northward advection of cooler water.

This paper is organized as follows. Section 2 describes the data and methods, including the regional ocean model set-up. Section 3 presents the model solutions, contrasting the late summer/early autumn 2011 evolution with the previous two years. We compare the simulated temperature evolution during the peak of the marine heat wave with observed data from an Integrated Marine Observing System mooring. From the model, a temperature budget is presented for the near-surface temperature evolution. Results are discussed and summarized in Section 4.

2. Data and methods

2.1. Regional model set-up

2.1.1. Model configuration

This study configures the Regional Ocean Modeling System (ROMS; Shchepetkin and McWilliams, 2005) for the study area. ROMS is an incompressible, hydrostatic, primitive-equation model with a free surface, horizontal curvilinear coordinate, and a generalized terrain-following vertical coordinate. The model domain covers the western coast of Australia from 21°S (North West Cape, the origin of the Leeuwin Current) to 35°S (Cape Leeuwin, where the Leeuwin Current starts to turn eastward into the Great Australian Bight) and 108°E to 116°E (see Fig. 1). The model has a grid dimension of 194 $\times$354 with horizontal resolution varying from 2 to 3.5 km from the coast line to 112°E and

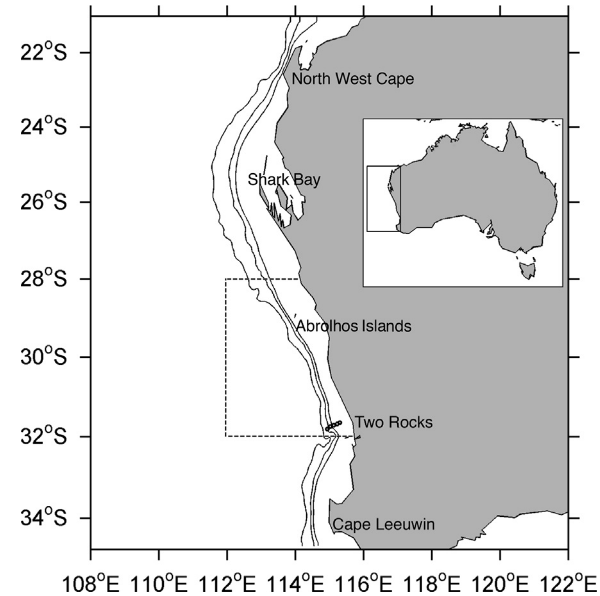

Fig. 1. Map of the model domain with inset showing location of the study area off Western Australia. The solid contour lines are isobaths of 200 m, 500 m and 1000 m. The dashed lines together with the coastline denote the surface area of a control volume for the temperature budget analysis. Circles are locations of the 5 moorings at the Two Rocks transect, namely TWR55, TWR105, TWR155, TWR205 and TWR505 from coast to offshore, and the numbers denote their nominal deployment depths.

increasing to 8 km at the oceanic open boundary. There are 30 σ-levels and the vertical resolution is refined in the top 100 m with the vertical stretching parameters $\theta_s = 7$ and $\theta_b = 0$. The bathymetry is based on Geoscience Australia 2005 bathymetric data at 0.005° resolution. The model's maximum and minimum depths are set to 2000 m and 30 m, respectively. After interpolation, the topography is smoothed so that slope factors are small enough to reduce pressure gradient errors. To smooth the topography, we use a linear programming (LP) procedure (Sikiric et al., 2009), followed by a Shapiro filter such that the Beckman and Haidvogel number (rx0) and the Haney number (rx1) are 0.2 and 3, respectively. The time step is 300 s.

2.1.2. Initial and boundary conditions

The ROMS model simulation was initialised with OceanMAPS, the Bureau of Meteorology's operational ocean prediction system with 10 km horizontal resolution in the Australian region and adjacent marginal seas, which developed from the BLUElink project (Oke et al., 2008). OceanMAPS uses the BLUElink Ocean Data Assimilation System (BODAS) to assimilate real-time, in-situ ocean observations (e.g., Argo, CTD (conductivity, temperature, depth) and XBT (expendable bathythermograph)) and remotely sensed sea level from satellite (e.g. Jason, Envisat). The model simulation is integrated from October 2007 (when OceanMAPS became operational) to June 2011. After about one year, the modelled volume-averaged kinetic energy oscillates around an equilibrium value. We analyse the model output from January 2009.

We also used OceanMAPS to provide the open boundary data for ROMS. At the three lateral open boundaries, an oblique radiation condition (Marchesiello et al., 2001) was used with a nudging term for tracers and velocities. If the direction of information flux is inward, the solution at the boundary is nudged quickly towards the values provided by OceanMAPS (timescale τ_{in}=1 day); otherwise the radiation condition is applied to extrapolate interior values at the boundary points and a weak nudging (timescale τ_{out}=30 days) is applied. The Flather (1976) boundary condition is used for the depth-averaged velocity and the Chapman (1985) condition for the sea surface level. A constraint on the depth-averaged velocities is also applied to enforce volume conservation. There are sponge and weak nudging layers in the outermost 6 grid cells of the model grid. Across the transitional zone from the inner edge to the boundary, horizontal viscosity and diffusivity increase linearly from 10 $m^2 s^{-1}$ to 50 $m^2 s^{-1}$, and the nudging strength also increases linearly from zero to its maximum. A non-local, K-profile parameterization (KPP) scheme (Large et al., 1994) is used for vertical mixing of momentum and tracers. Away from the transitional zone, Laplacian horizontal mixing is applied with the horizontal viscosity and diffusivity equal to 10 $m^2 s^{-1}$.

2.1.3. Model forcings

The surface forcing of momentum, heat and freshwater fluxes are derived from the global version of the Australian Community Climate and Earth-System Simulator (ACCESS-G; 80 km resolution) (Australian Bureau of Meteorology, 2010). The net surface heat flux Q_{net} is the sum of solar radiation, longwave radiation, latent and sensible heat fluxes. A correction term with respect to OceanMAPS SST is introduced to represent thermal feedback of the SST to the flux at the air–sea interface (cf. Marchesiello et al., 2003). The total heat flux (sum of Q_{net} and the correction term) is applied to the surface grid cell; however the solar radiation flux is treated separately and is allowed to penetrate into water columns with exponential decays as the first Jerlov water type (Paulson and Simpson, 1977).

Fig. 2 presents a time-series of spatially averaged total heat flux and meridional wind stress. The total heat flux is partitioned into offshore (110°E to 114°E; 32°S to 28°S; Fig. 2a) and near-coastal (114°E to the coast; 32°S to 28°S; Fig. 2b) regions. In February 2011, the marine heat wave coincided with a positive peak in total heat flux offshore (Fig. 2a) and weakened southerly winds (Fig. 2c). The mean total heat flux in February 2011 shows anomalously positive heat flux into the ocean (Fig. 3b and c) compared to the average flux from the previous two years (Fig. 3a). We will explore the 2011 anomalous heat flux's contribution to spatial patterns of warming using the model simulation.

2.2. Data sets used for model evaluation

2.2.1. TMI sea surface temperature

To evaluate the model solutions for sea surface temperature (SST), we use the daily Tropical Rainfall Measuring Mission (TRMM) Microwave Imager (TMI) SST (Wentz, 1997). TMI SST provides daily SST at 0.25° × 0.25° resolution. We use SST from the time period of interest, i.e. 2009–2011. Data is not provided near the coastline, corresponding to approximately onshore of 250 m depth in the model.

2.2.2. IMOS moorings: two rocks transect

Established in 2007, the Integrated Marine Observing System (IMOS) has deployed a range of observing platforms in the oceans around Australia and the data is openly available online. IMOS started its monitoring program of the LC system using shelf moorings in 2009. There are five mooring stations at the Two Rocks transect (see Fig. 1), namely TWR55, TWR105, TWR155, TWR205, TWR505 which are deployed at water depths of 55 m, 105 m, 155 m, 205 m and 505 m, respectively. Mooring data at these five stations will be used for model comparison (Section 3.3) and validation (Appendix A).

3. Results

We first describe the observed and modelled evolution of the sea surface temperature (SST) during the austral summer of 2011, which shows a dramatic increase in temperature along the entire shelf of Western Australia (Section 3.1). The near-surface velocity field is presented to illustrate the changes in velocity during this time period (Section 3.2). We compare the model's thermal and

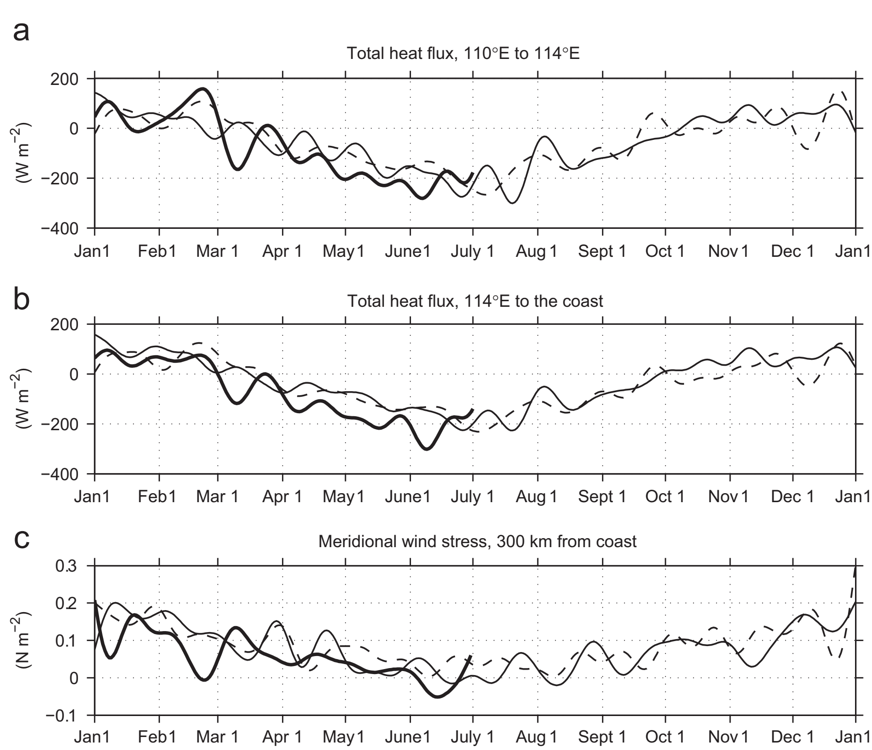

Fig. 2. Time series of the spatially-averaged (a) total heat flux offshore of the shelf (110°E to 114°E; 32°S to 28°S), (b) total heat flux near the coast (114°E to the coast; 32°S to 28°S), and (c) meridional wind stress (from the coast to 300 km offshore; 32°S to 28°S). The curves are for 2009 (thin, solid line), 2010 (dashed line), and 2011 (thick, solid line). The 2011 curve is truncated where the simulation ends. Daily-averaged fields are low-pass filtered (6th-order Butterworth filter, 0.05 day^{-1} cut-off frequency).

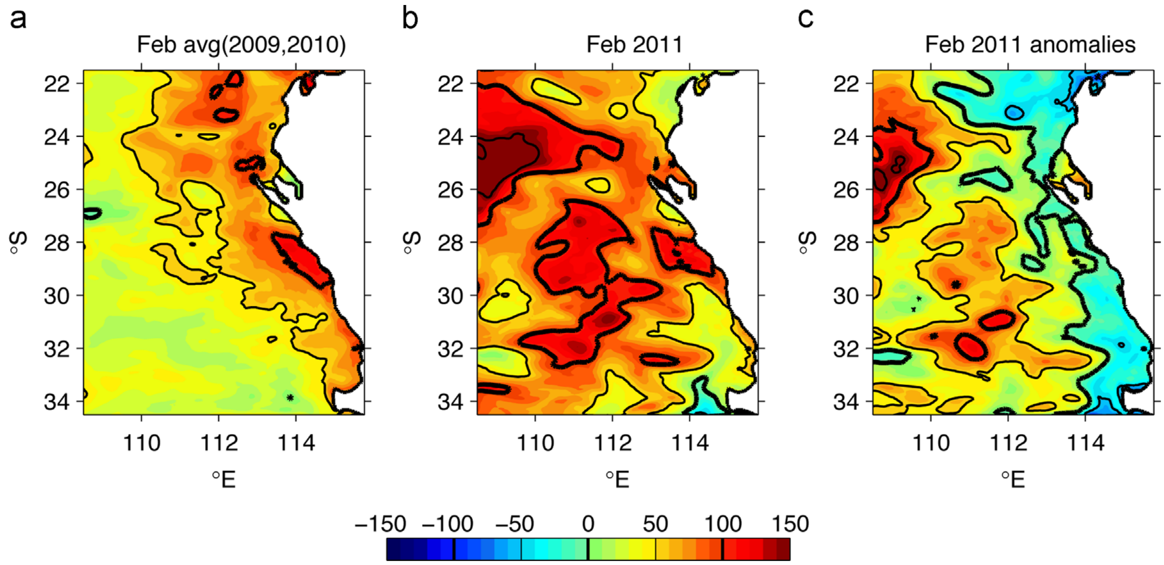

Fig. 3. The time-averaged total heat flux (W m^{-2}) (a) in February 2009 and 2010, (b) in February 2011, and (c) corresponding anomalies (February 2011–February 2009, 2010). The heat flux is contoured every 50 W m^{-2} with thick solid lines for −100, 0, 100 W m^{-2}.

velocity evolution at the Two Rocks site (Section 3.3). Then, a temperature budget is presented for the upper 60 m to quantify the mechanisms responsible for the warming in the boxed domain shown in Fig. 1 (Section 3.4). Finally, we present an analysis of dynamical links between remote and local forcings with the flow field to explain the anomalous temperature rise during this time period (Section 3.5).

3.1. Evolution of the marine heat wave from SST

The peak of the marine heat wave occurred in late February–early March 2011 (Feng et al., 2013; Pearce and Feng, 2013). Fig. 4 (top panels) provides maps of model SST, which are time-averaged over the 20-day period from February 19 to March 10 during 2009–2010 (time mean; left panels) and 2011 (middle panels). In a 5°-wide region off the west coast of Australia, the SST isotherms are shifted southward by 5–10° during the peak of the marine heat wave in 2011. The model SST patterns agree with the overall pattern revealed by the time-mean TMI SST (bottom panels). This agreement supports our use of the model to analyse the causes of the magnitude and spatial structure of the warming event. The difference between the two time periods (right panels) reveals large regions along the shelf where the warming is greater than 5 °C. At the offshore edge of the domain from 27°S to 30°S, the model tends to overestimate the SST. However, this overestimation does not impact the heat budget analysis near the coast. In summary, off the mid-west WA shelf, the model well reproduces the timing and amplitude of the warming.

Fig. 5 plots time series of the mean SST off the west coast in the boxed domain shown in Fig. 1. The plots show that SST was already anomalously warm by 1–1.5 °C at the start of 2011 compared to the previous two years. From the model, the mean SST rapidly increased 3.6 °C from February 1 to March 1, the peak in SST. The mean SST from TMI followed a similar rapid increase of 3.5 °C during February 2011. Both time series depict a rapid rise in SST over February 2011, with a slower fall in temperature after its peak.

To examine spatial patterns of the rise and fall of the temperature peak, Fig. 6 shows temperature and sea level anomalies for the six 20-day periods from January 1 to April 30. The thermal and sea level anomalies are defined by the difference in their values during 2011 from the previous two years (time mean, 2009–2010) during the same time period. The warm temperature anomalies are associated with anomalously high sea level. Near the coast, anomalously high sea level occurs during all time periods. This high sea level corresponds with anomalous poleward flow at the surface, which is intensified in regions where the sea level anomaly contours are more closely spaced such as near the coast at the peak of the event in Fig. 6c. In January, the warm SST anomaly is predominantly located between the North West Cape and Shark Bay, and it propagates poleward in February. In mid-February, the peak in warm anomaly is present over the entire coast with another peak offshore.

After the peak of the heat wave on March 1, positive sea level anomalies detach from the coast and propagate offshore along with the warm anomalies, likely following the propagation of mesoscale eddies. Near the coast and within the positive sea level anomalies, the magnitude of the warm anomalies tends to decay in time. The offshore spread of warm anomalies tends to be consistent with other modelling studies, in which eddy heat fluxes are shown to transfer heat offshore from the coast (Domingues et al., 2006). Observations indicate that long-lived, anticyclonic, warm-core eddies are known to drift offshore along the 28°S to 32°S corridor (Fang and Morrow, 2003) as seen in the model results. The Leeuwin Current eddies tend to strengthen in austral winter under normal conditions. The Leeuwin Current eddy structures in austral summer captured by the model simulation suggest it is related to the unusual conditions of the 2011 Ningaloo Niño.

3.2. Velocity field: time-evolution of the Leeuwin Current and Capes Current

To determine how changes in the circulation contributed to the intense warming in 2011, Figs. 7 and 8 present maps of the model's velocity field. Velocity is depth-averaged over the upper 250 m, a typical estimate of the Leeuwin Current depth (e.g. Feng et al., 2003, 2008). As in Fig. 4, the maps compare two time periods, 2011 and a time-average of 2009–2010 for each of the six 20-day periods. From January through April, the depth-averaged velocity is dominated by eddies off the west coast of Australia, but several large-scale features are notable. The LC tends to flow poleward south of Shark Bay to Cape Leeuwin, following topography offshore of the 100 m isobath. Overall speeds in 2011 are notably greater than the average of the previous two years. In February 2011, prior to the peak in SST, LC speeds intensified, with peak

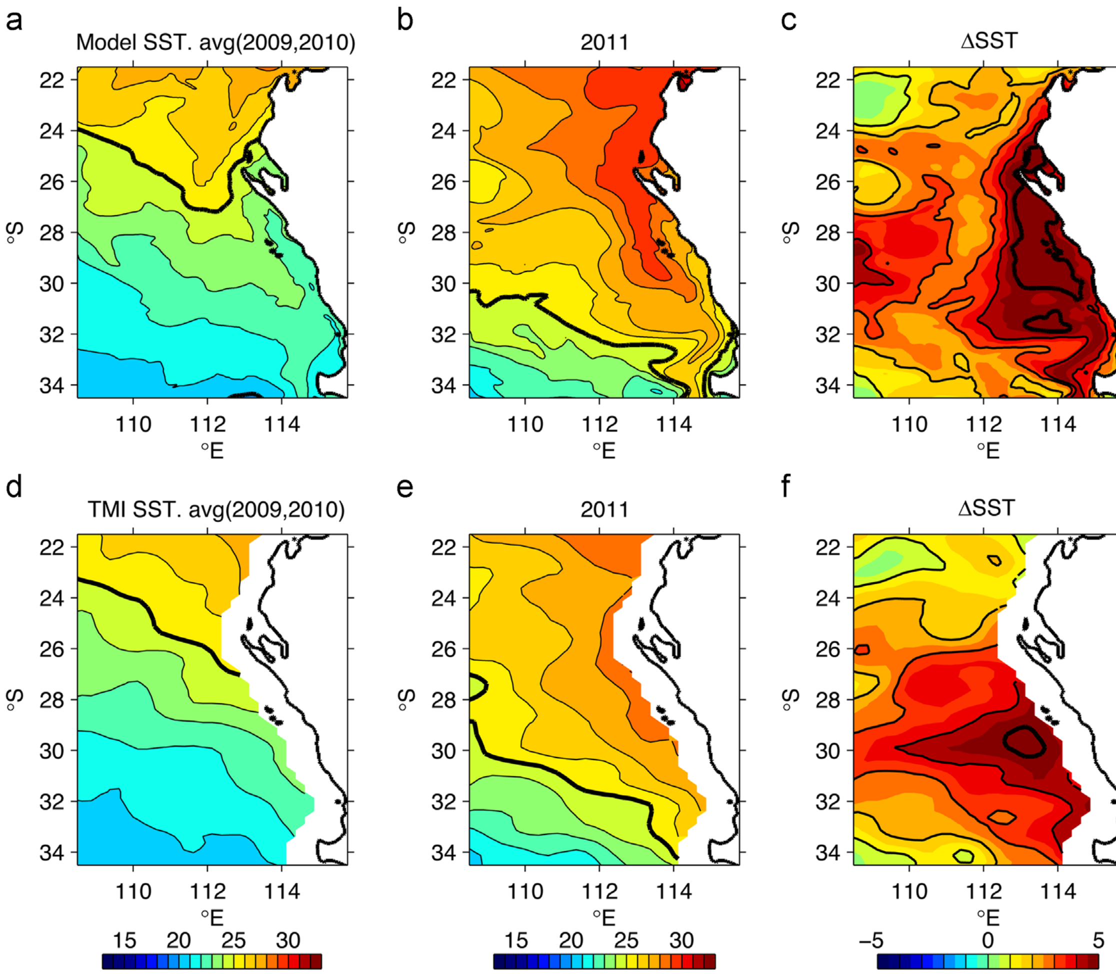

Fig. 4. The sea surface temperature (SST) from February 19 to March 10 (20 day average). The top panels (a,b,c) are from the model SST and the bottom panels (d,e,f) are from the TMI SST. The left panels are the time-averaged SST from 2009 to 2010, the middle panels are from 2011 (i.e. the peak of the marine heat wave), and the right panels are the SST difference, between the two time periods. The SST is contoured every 1 °C and the thick black contour is for 25 °C in (a,b,d,e) and 5 °C in (c,f).

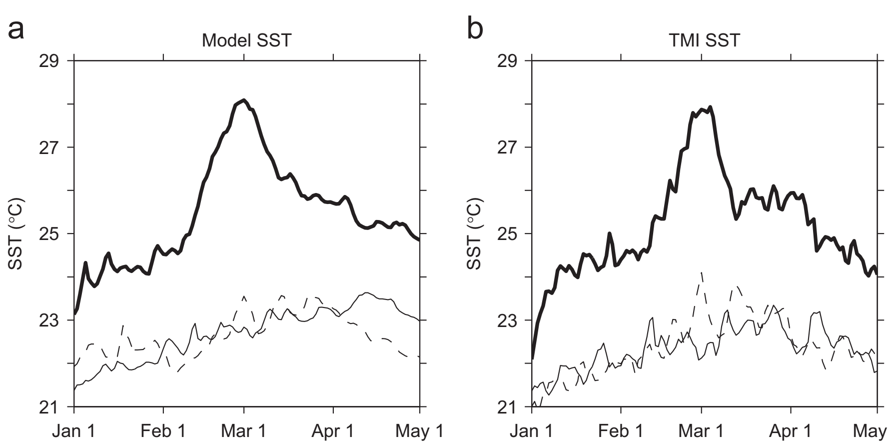

Fig. 5. The mean SST within the region enclosed by dashed lines in Fig. 1 (32°S to 28°S, and 112°E to the coast). The (a) model SST and (b) TMI SST. The curves are for 2009 (thin, solid line), 2010 (dashed line), and 2011 (thick, solid line).

speeds offshore of the Abrolhos Islands and south of Perth (Fig. 7f). This striking poleward current breaks up into eddies following the peak (Fig. 8d), resulting in alternating bands of eastward and westward flows south of the Abrolhos Islands. Subsequently, the poleward current reemerges in mid-March to early-April (Fig. 8e), with intensified meandering and eddy activity in April (Fig. 8f).

The Capes Current flows equatorward over the continental shelf (inshore of the 100 m isobath) from Cape Leeuwin to Shark Bay from January through March during 2009 and 2010 (Figs. 7 and 8). This equatorward flow usually emerges during these months and is associated with upwelling and advection of cooler water northward (e.g. Woo et al., 2006). In 2011, however, a

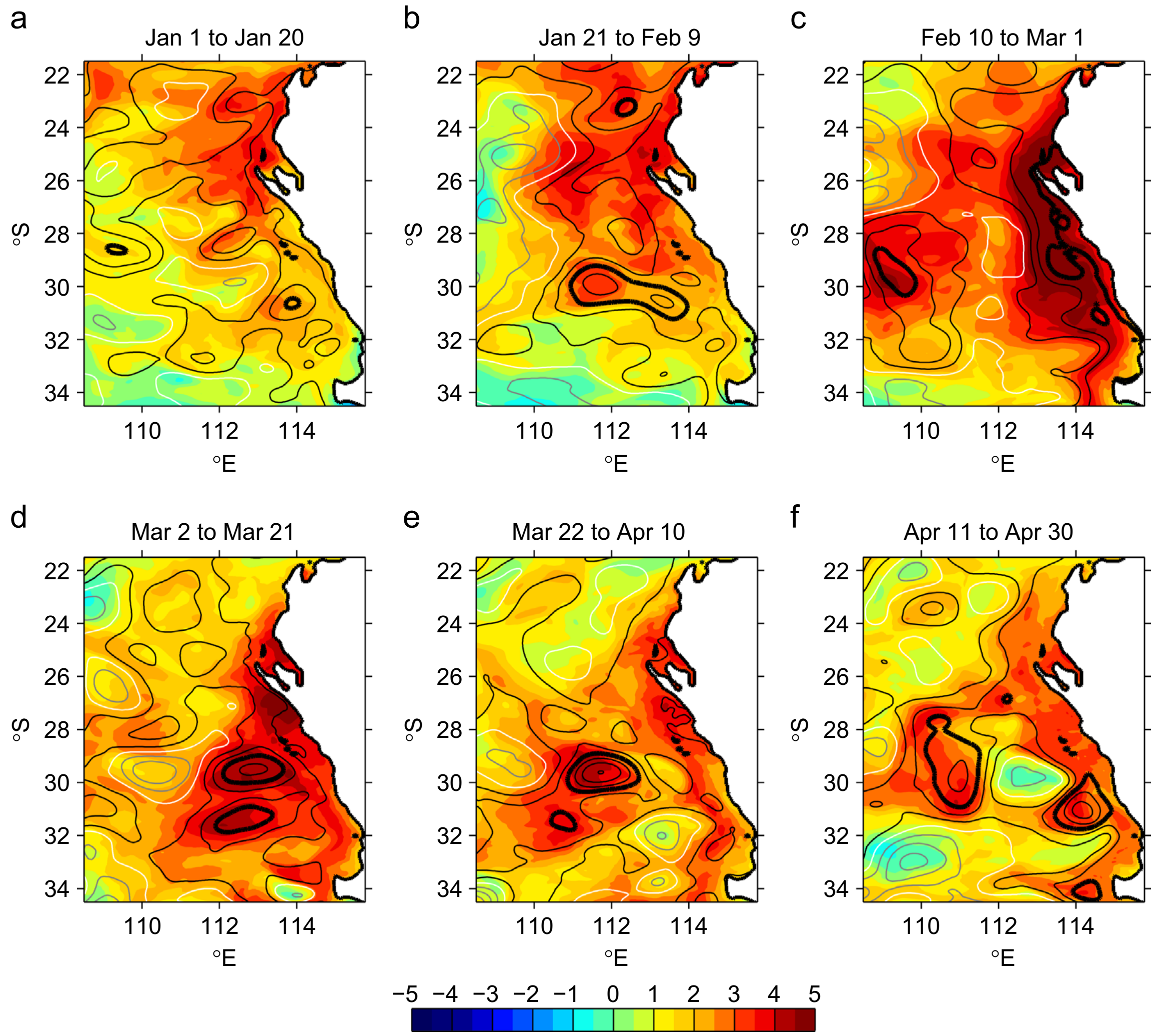

Fig. 6. The model's SST and surface elevation anomalies time-averaged over 20 day periods for the rise (top panels) and fall (bottom panels) of the 2011 marine heat wave. The SST anomaly (shaded) is the difference between the SST in 2011 and the mean SST during the same time period in 2009, 2010. The sea level anomaly (lines) is contoured every 0.1 m for positive (black lines) and negative (grey lines) values, where the zero contour is included (white lines). The thick black line is for +0.3 m sea level anomaly.

coherent equatorward flow over the shelf is disrupted by mesoscale activity. Prior to the peak of the marine heat wave, the CC appears completely suppressed with poleward flow over the shelf from the North West Cape to Cape Leeuwin (Fig. 7f). After the peak, the current over the shelf flows equatorward but again reverses to a weak, poleward flow in mid-March to early-April (Fig. 8d and e).

The intensification of the LC and the suppression of the CC in February 2011 have important consequences for the temperature field. The intensified LC advects warm water southward, contributing to the peak in SST. The suppression of the CC inhibits upwelling and equatorward advection of cooler water. Instead, the anomalous poleward flow over the shelf contributes to warming there, in contrast to previous years. In Section 3.5, we explore how local and remote wind forcing are related to these changes in the coastal currents, which subsequently impact temperature advection.

3.3. Temperature and meridional velocity at the Two Rocks transect

The IMOS moorings deployed at the Two Rocks transect have data including the peak of the marine heat wave. Fig. 9a and b compares the IMOS TWR205 data and ROMS model in 2011. The meridional velocity in the upper 200 m shows similar poleward acceleration in the LC prior to the peak in temperature. Mean speeds reach over 0.5 cm s^{-1} throughout the upper 200 m.

From IMOS TWR155, the temperature profile shows a rapid warming in February 2011 with a peak in March (Fig. 9c). The ROMS model captures the dominant features of the evolving thermal stratification and the timing of the temperature peaks (Fig. 9d). The stratification is weak in austral spring 2010 and becomes stronger in the summer of 2010–2011. The modelled stratification is close to the observed one, but with a warm bias almost uniformly in the water column (see Fig. 15a). The profiles indicate that the warming is surface-intensified, over the upper 60 m, consistent with an offshore Argo profile (see Fig. 6h and i in Feng et al., 2013). Appendix A provides additional model comparison and validation. Since the data and model agree in the timing of the poleward current's acceleration and temperature peak, we use a near-surface temperature budget to quantify the mechanisms contributing to the warming event.

3.4. Near-surface temperature budget off Western Australia

3.4.1. Depth-averaged temperature budget

The mechanisms contributing to the peak in near-surface warming are analysed using a temperature budget over the upper 60 m. The time rate of change in temperature T is

$$\frac{\partial T}{\partial t} = -\mathbf{u}\cdot\nabla T + \nabla_H\cdot(\kappa_H \nabla_H T) + \frac{\partial}{\partial z}\left(\kappa_V \frac{\partial T}{\partial z}\right), \qquad (1)$$

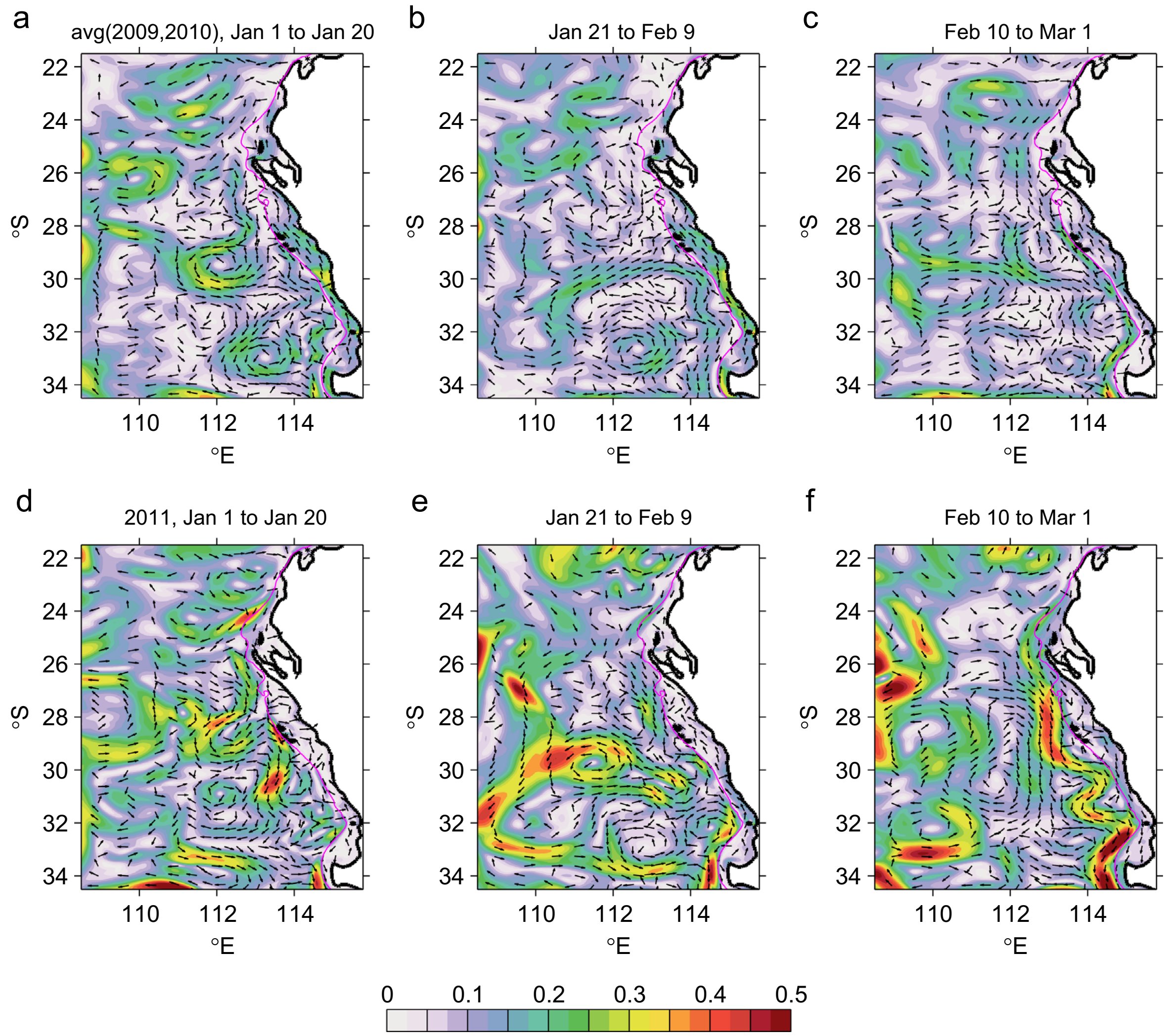

Fig. 7. The model's depth-averaged velocity (0–250 m) over three 20-day period from January 1 to March 1 (rise of the marine heat wave peak). The top panels show the velocity field in 2009, 2010 (time-averaged) and the bottom panels show the velocity in 2011. The speed (m s^{-1}) is shaded and the arrows indicate the velocity direction. The 100 m isobath (pink curve) is included for reference. (For interpretation of the references to colour in this figure caption, the reader is referred to the web version of this paper.)

where ∇_H is the horizontal (x, y) gradient operator, $\kappa_H = 10$ m^2 s^{-1} is the horizontal diffusivity, and κ_V is the vertical diffusivity determined by KPP. Then, the temperature equation is depth-averaged over a depth H and integrated in time over a time period Δt. We refer to this depth-averaged temperature as the near-surface temperature. The depth- and time-integrated temperature equation becomes

$$\underbrace{\frac{1}{H}\int^{\Delta t}\int^{H}\left(\frac{\partial T}{\partial t}\right)dz\,dt}_{\Delta T_{TOTAL}} = \underbrace{-\frac{1}{H}\int^{\Delta t}\int^{H}(\mathbf{u}\cdot\nabla T)\,dz\,dt}_{\Delta T_{ADV}} + \underbrace{\frac{1}{H}\int^{\Delta t}\int^{H}\nabla_H\cdot(\kappa_H\nabla_H T)\,dz\,dt}_{\Delta T_{HDIFF}} + \underbrace{\frac{1}{H}\int^{\Delta t}\int^{H}\frac{\partial}{\partial z}\left(\kappa_V\frac{\partial T}{\partial z}\right)dz\,dt}_{\Delta T_{Q}}, \qquad (2)$$

where H=60 m or the water depth onshore of 60 m, ΔT_{TOTAL} is the total near-surface change in temperature, ΔT_{ADV} is the near-surface change in temperature due to advection, ΔT_{HDIFF} is the near-surface change in temperature due to the horizontal diffusion, and ΔT_Q is the near-surface change in temperature due to the total air–sea heat flux Q ($Q > 0$ is warming) and vertical turbulent flux. When integrated over the entire water column depth, the vertical diffusion term is controlled by the total air–sea heat flux because there is no diffusive flux at the bottom.

Fig. 10 plots maps of the above terms determined from the model output from January 1 to March 1 (Δt = 60 days) for each year. The term ΔT_{HDIFF} is negligible (absolute values on the order of 0.1 °C) and so is not shown. In 2009 and 2010, the total change in near-surface temperature offshore of 100 m depth is positive (Fig. 10a and d), and in 2010 there is cooling over the continental shelf adjacent to the coast. Total advection of temperature contributes to warming offshore. Near the coast, sustained equatorward flow by the CC, and coastal upwelling lead to a net cooling that extends from Cape Leeuwin to Shark Bay in both 2009 and 2010 (Fig. 10b and e). The weaker LC during the 2009–early 2010 El Niño event also contributed to the cooling from Cape Leeuwin to the North West Cape (Fig. 10e). Positive air–sea heat flux into the ocean contributes to offshore warming and tends to counteract the cooling by advection near the coast (Fig. 10c and f).

In 2011, the total change in near-surface temperature shows intense warming both offshore and on the continental shelf, exceeding 5 °C in large areas (Fig. 10g). Total advection contributes to a significant part of this net warming (Fig. 10h). In contrast to

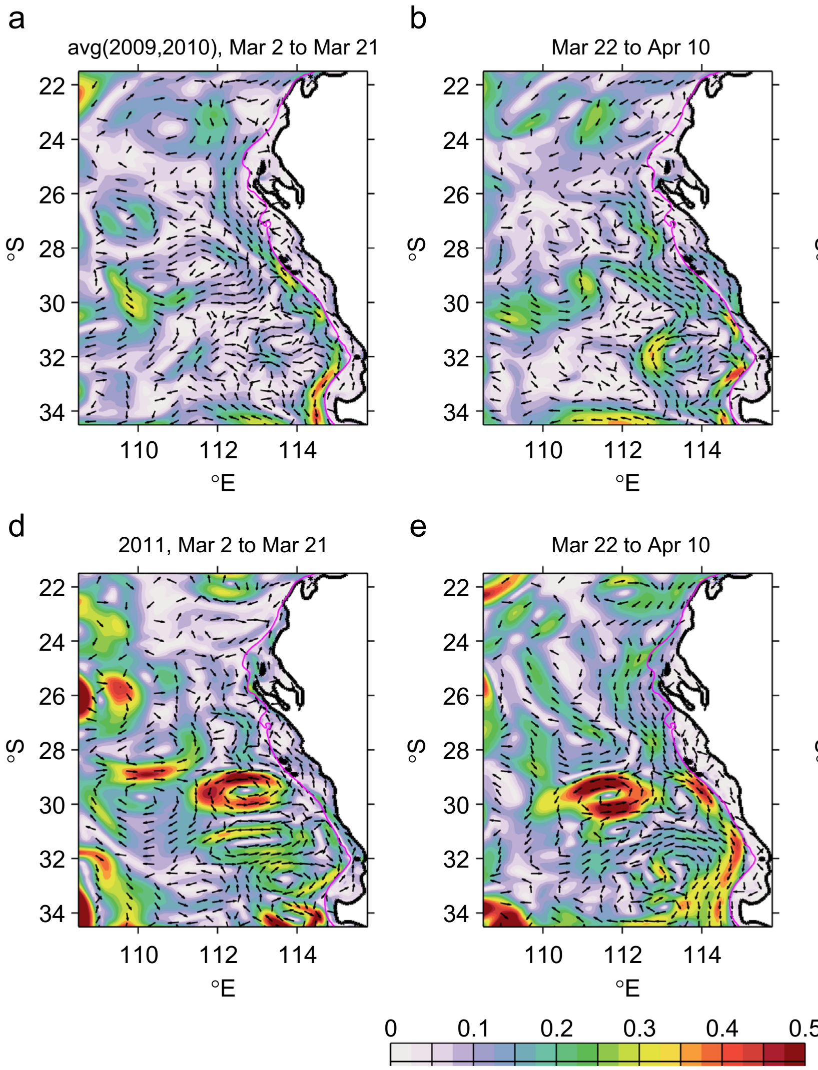

Fig. 8. The model's depth-averaged velocity (0–250 m) over three 20-day periods from March 2 to April 30 (fall of the marine heat wave peak). The panels follow from Fig. 7, where speed (m s^{-1}) is shaded.

2009 and 2010, advective cooling in the near-surface temperatures next to the coast is suppressed in 2011. Instead, total advection tends to warm waters onshore of ~ 100 m although the warming is more intense offshore. Regions such as Exmouth Gulf, Shark Bay, and onshore of the Abrolhos Islands appear sheltered from advective warming. Near the coast, warming over the shelf owing to air–sea heat flux into the ocean is similar in magnitude and spatial pattern as in 2009 and 2010. On the other hand, widespread warming due to air–sea heat flux is apparent offshore of the continental shelf (Fig. 10i).

3.4.2. *Volume-averaged temperature budget*

To quantify the relative contributions to the intense warming shown by these spatial patterns, we averaged (1) over a volume V, defined by a depth $H=60$ m and an area A from 32°S to 28°S and 112°E to the coast (see boxed domain in Fig. 1), to get

$$\underbrace{\frac{1}{V}\int^{V}\left(\frac{\partial T}{\partial t}\right)dV'}_{RATE_V} = \underbrace{-\frac{1}{V}\int^{V}(\mathbf{u}\cdot\nabla T)\,dV'}_{ADV_V} + \underbrace{\frac{1}{V}\int^{V}\frac{\partial}{\partial z}\left(\kappa_V\frac{\partial T}{\partial z}\right)dV'}_{Q_V}, \quad (3)$$

where $RATE_V$ is the time-rate of change in the volume-averaged temperature, ADV_V is the time-rate of change in volume-averaged temperature due to total advection, and Q_V is the time-rate of change in volume-averaged temperature due to the air–sea heat flux through vertical diffusion. We neglect horizontal diffusion because its contribution is negligible.

Fig. 11 plots the time-rate of change of each term during January to May, 2009–2011. In 2009 and 2010, $RATE_V$ is predominantly due to air–sea heat fluxes, Q_V (Fig. 11a and b). From January 1 to March 1, the time-rate of change due to advection, ADV_V, is either near zero (2009) or negative (2010). In contrast, in 2011, $RATE_V$ has contributions from both advection and air–sea heat flux (Fig. 11c). In February 2011, ADV_V dominates the positive rate of change with a peak in mid-February. After March 1, both ADV_V and Q_V decay to zero and then reverse sign. Thereafter, $RATE_V$ is controlled by Q_V, which tends to cool the region. During April, ADV_V contributes positively but does not completely counteract the negative rate of change due to Q_V.

Fig. 12 plots time integrals of each of the curves in Fig. 11 from January 1 of each year. From January 1st, the volume-averaged temperature changes by a maximum $+2$ °C in 2009 and 2010 (Fig. 12a and b). This positive change is mainly due to air–sea heat fluxes. In 2010, advection tends to oppose this net positive change, cooling this region, likely due to the prevailing El Niño conditions. In 2011, advection and air–sea heat fluxes tend to equally contribute to a positive change in temperature until early February (Fig. 12c). In February, advection leads to a rapid increase in the

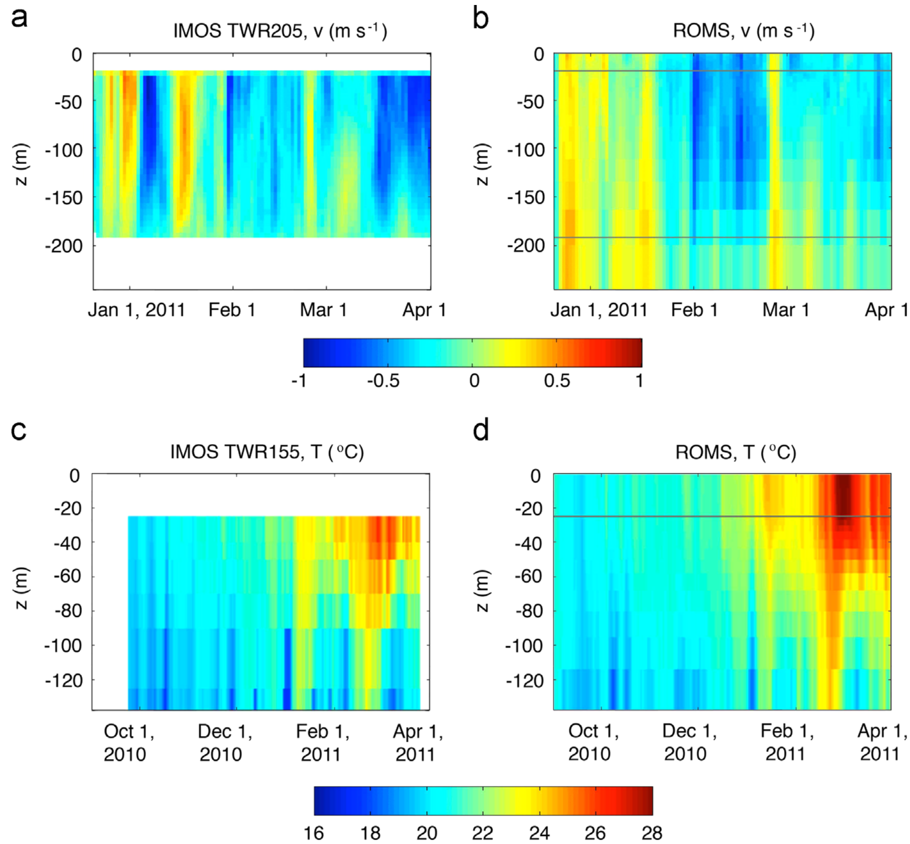

Fig. 9. (Top panels) The time evolution of the meridional velocity profiles from (a) the IMOS mooring TWR205 and (b) the corresponding location from the ROMS solution. (Bottom panels) The time evolution of temperature profiles from (c) the IMOS mooring TWR155 and (d) the ROMS solution. The grey lines in (b,d) are included for reference.

temperature change, surpassing +2 °C by mid-February and peaking at +4.2° on March 5. Subsequently, the temperature change due to Q_V decreases while the temperature change due to ADV_V does not significantly vary. Hence the temperature change's peak is asymmetric, with a steep rise in temperature prior to the peak and slower decay after the peak, a feature also reflected in both model and TMI SST (Fig. 5).

We can quantify the relative contributions to the net change in temperature at the peak of the marine heat wave. On March 1, 2011, the volume-averaged, time-integrated change in temperature is a total +4.1 °C, where +2.7 °C is the contribution from advection and +1.4 °C is the contribution from air–sea heat flux. Thus, advection is responsible for ≈2/3 of the warming and air–sea heat flux contributes ≈1/3. The peak in the net change in temperature over this volume occurs on March 5 rather than March 1 (peak in SST), reflecting an approximate one-week time-lag in sub-surface changes. The peak temperature change is +4.2 °C, where advection contributes +2.8 °C and air–sea heat flux contributes +1.4 °C. The March 1 temperature change is markedly different in 2009 and 2010. On March 1, the mean change for these years is only +1.4 °C, where advection contributes only −0.1 °C and air–sea heat flux contributes +1.5 °C. Thus, on average, advection contributes to less than 10% of the change in temperature in 2009 and 2010. Therefore, the remarkably strong advection in 2011 is responsible for a large part of the warming off Western Australia.

3.5. Dynamical links between coastal currents and wind forcing

The impacts of remote wind and local wind forcing are investigated to quantify their roles in the anomalous temperature advection leading to the temperature peak in 2011.

3.5.1. Remote forcing

The 2010–2011 La Niña was associated with anomalous easterly winds in the tropical Pacific Ocean. The remote winds led to deepening of the warm pool in the Western Pacific Ocean and, along the coastal waveguide, caused the associated high steric heights and deeper thermocline depths to propagate through the Indonesian Seas into the Eastern Indian Ocean (Feng et al., 2003). The Fremantle sea level anomalies are correlated with the remote wind forcing at time-lag of about a month (Feng et al., 2013).

Because of the Indian Ocean's tight dynamical links with the Pacific Ocean, changes in the thickness of the warm water region in the Eastern Indian Ocean can be used as a measure of the influence of remote forcing from the Pacific Ocean. During La Niña periods, the thermocline deepens as warm water enters into the Indian Ocean (Feng et al., 2003). Past studies have used the 20 °C isotherm depth as a proxy for thermocline variations in the Indian Ocean (e.g., Shinoda et al., 2004; Bracco et al., 2005; Singh et al., 2013). Recent modelling studies of the LC (Furue et al., 2013; Benthuysen et al., 2014) demonstrate how changes in the upper ocean density field north of the LC can impact the LC transport. The upper ocean density field supports a geostrophic, near-surface eastward flow that interacts with the LC. When the pycnocline deepens, the LC speed and transport intensifies. This intensification is caused by topographic trapping of Rossby waves over the slope and a net convergence in the eastward transport onto the slope. In these modelling studies, the upper layer is associated with the 1026 kg m^{-3} isopycnal, which captures variations in both salinity and temperature. The variations in the 1026 kg m^{-3} isopycnal depth can reflect changes associated with ENSO variability, similar to using the 20 °C isotherm depth.

Fig. 13a and b plot maps of the depth of the 1026 kg m^{-3} isopycnal from the model, averaged from January 1 through April

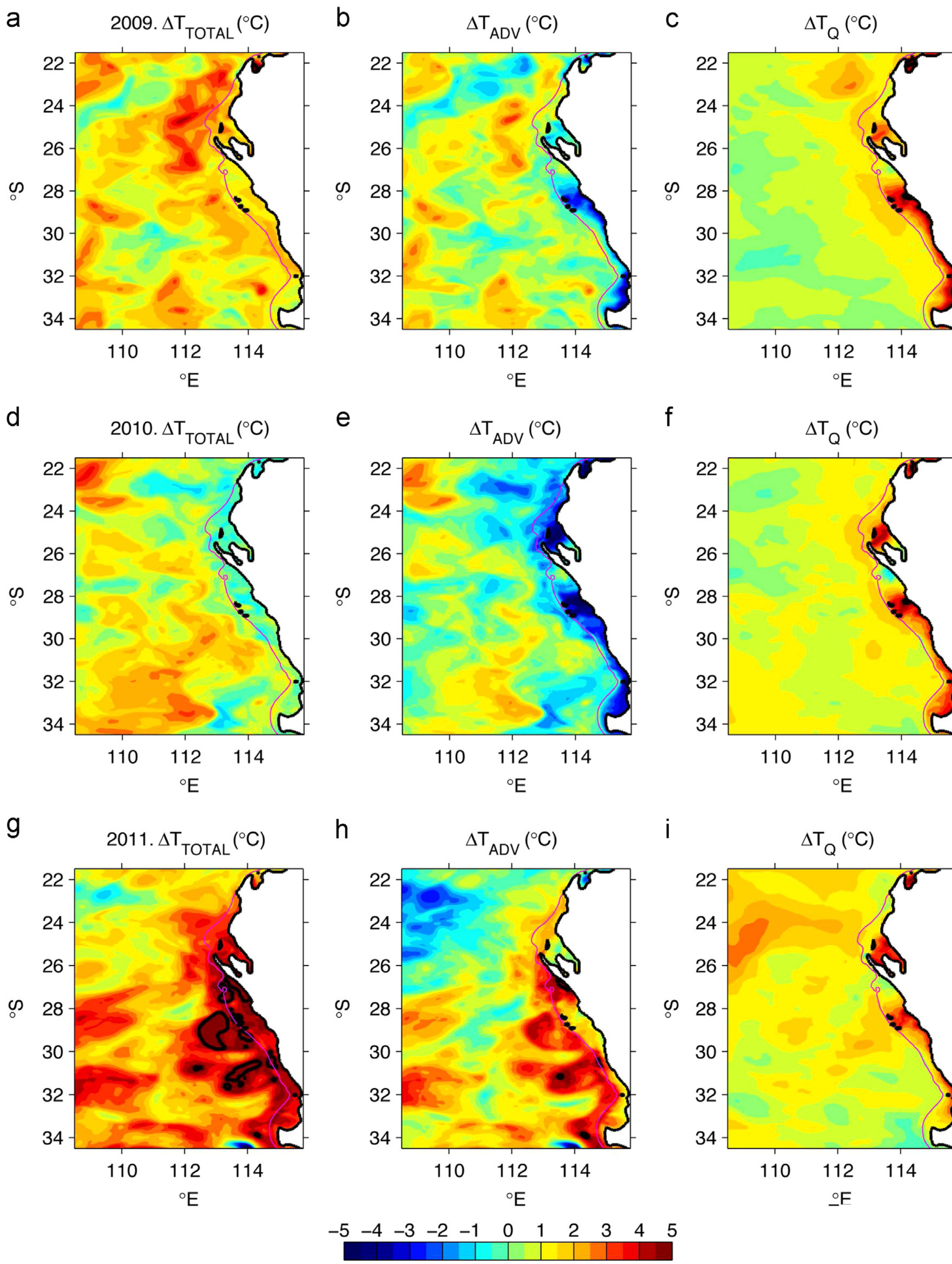

Fig. 10. The model's change in depth-averaged temperature ($H=60$ m) from January 1st to March 1st in 2009 (top panels; a,b,c), 2010 (middle panels; d,e,f), and 2011 (bottom panels, g,h,i). The terms correspond to the temperature budget in Eq. (2), where horizontal diffusion is negligible. The left to right panels show the total change in temperature, ΔT_{TOTAL} (a,d,g), the change due to advection, ΔT_{ADV} (b,e,h), and the change due to the air–sea heat flux via turbulent diffusion, ΔT_{Q} (c, f, i). The region where the change in temperature is greater than 5 °C is contoured with the thick black contour. The pink curve is the 100 m isobath. (For interpretation of the references to colour in this figure caption, the reader is referred to the web version of this paper.)

30. The isopycnal depth is deepest ($\approx$240–300 m) near the coast which is likely due to poleward wave propagation from the north. The change in depth between the two time periods (2009–2010 and 2011) reveals that the 1026 kg m^{-3} isopycnal depth was deeper nearly everywhere in 2011. The deepening reached 30–40 m in the northern part of the domain and as much as 100 m near 31°S (Fig. 13c). Early 2010 was an El Niño period, which would correspond to shallower "upper layer" depths, so this change in depth may be greater than compared with normal conditions.

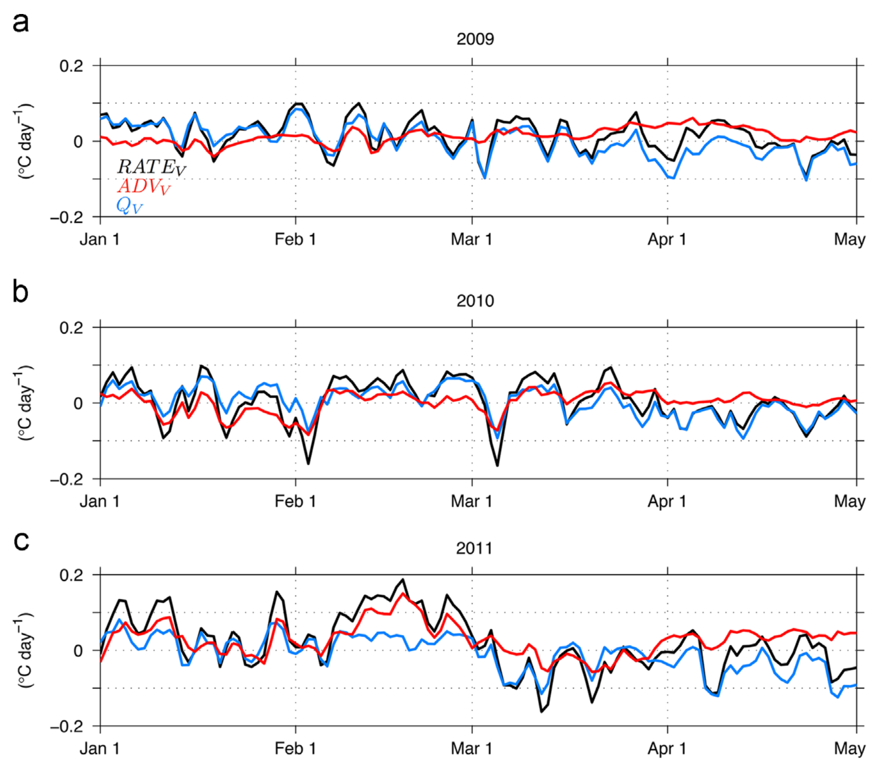

Fig. 11. Terms in the model's volume-integrated temperature equation (3) for (a) 2009, (b) 2010, and (c) 2011. The terms show the total time-rate of change in volume-integrated temperature, $RATE_V$, (black line), which is the sum of the rate of change due to total advection, ADV_V, (red line) and the rate of change due to air–sea heat flux through vertical diffusion, Q_V (blue line). (For interpretation of the references to colour in this figure caption, the reader is referred to the web version of this paper.)

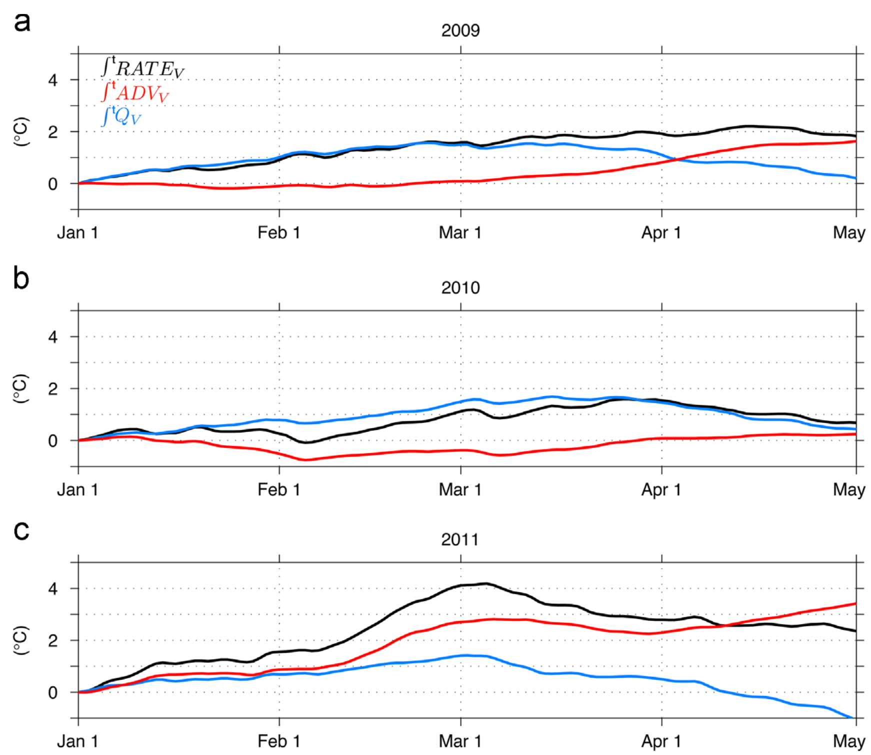

Fig. 12. Terms in the volume- and time-integrated temperature equation (3) for (a) 2009, (b) 2010, and (c) 2011. The terms are time-integrated from January 1st of each year. From this start date, the terms show the net change in volume-integrated temperature (black line), which is the sum of the change due to total advection (red line) and the change due to air–sea heat flux through vertical diffusion (blue line). (For interpretation of the references to colour in this figure caption, the reader is referred to the web version of this paper.)

3.5.2. Local and remote forcing and the boundary current transports

To identify the links among local and remote forcings and the Leeuwin and the Capes Current, Fig. 14 plots pairs of temporally and spatially averaged variables from the boxed domain in Fig. 1. For each six 20-day time period (January 1–April 30), the meridional flow is depth-integrated to 250 m depth and zonally

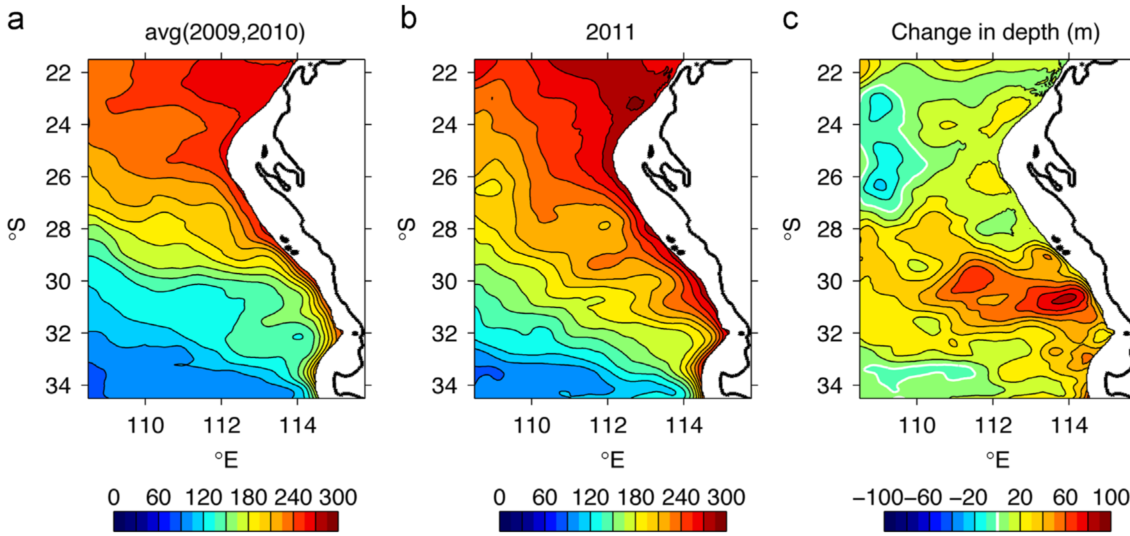

Fig. 13. Depth (m) of the 1026 kg m^{-3} isopycnal time-averaged from January 1st through April 30th for (a) 2009–2010 (time-averaged) and (b) 2011. The depths are contoured every 15 m. (c) The change in depth (m), i.e. depth in (b)–depth in (a). Depths are contoured every 10 m and the zero contour is indicated by the white line. The white region over the continental shelf is where potential density is less dense than 1026 kg m^{-3}.

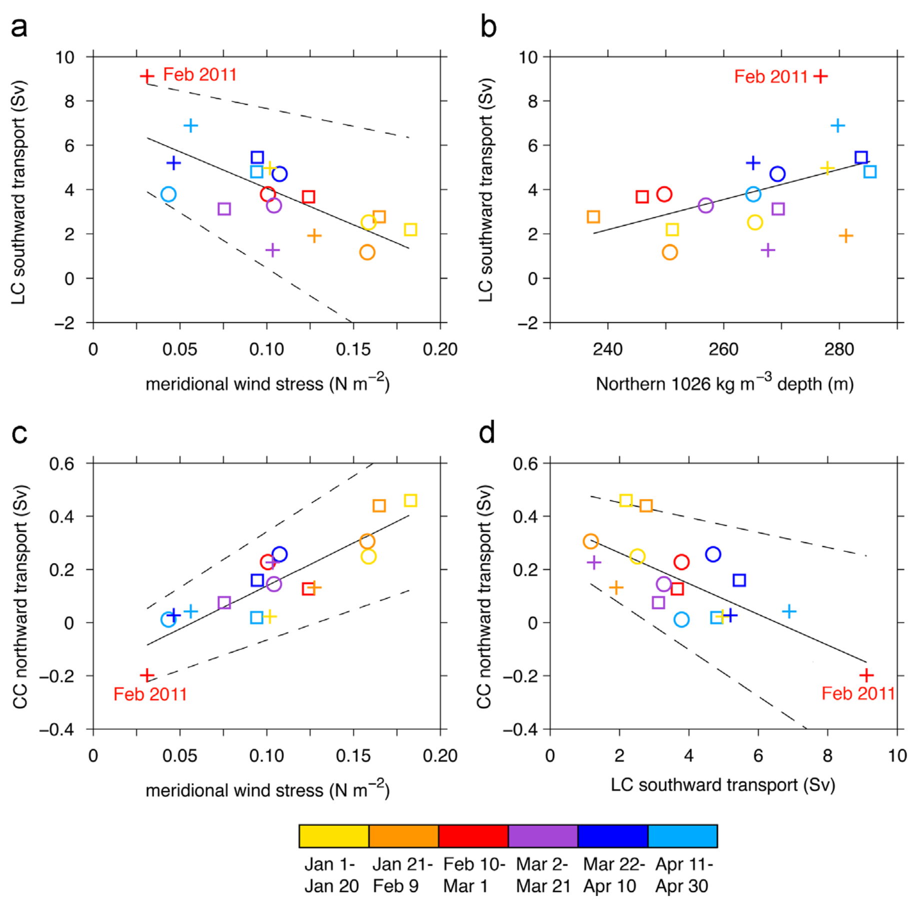

Fig. 14. The model's Leeuwin Current (LC) and Capes Current (CC) transports are plotted against remote and local wind forcing for each 20-day period. (a) The LC transport (averaged from 32°S to 28°S) versus the meridional wind stress (averaged from 300 km to the coast and 32°S to 28°S). (b) The LC transport versus the Northern depth of the 1026 kg m^{-3} isopycnal (averaged from 22°S to 24°S and over 2° offshore of the coast). (c) The CC transport (averaged from 32°S to 28°S) versus the meridional wind stress (averaged from 100 m depth to the coast and 32°S to 28°S). (d) The CC transport versus the LC transport. The symbols indicate time periods during 2009 (□), 2010 (○), and 2011 (+). The colours correspond to the time periods indicated in the colourbar and red is indicated as "Feb 2011" in the plot. The best-fit linear curve (solid lines) and 95% confidence intervals (dashed lines) are plotted. In (b), the 95% confidence bounds are outside of the plotted domain. (For interpretation of the references to colour in this figure caption, the reader is referred to the web version of this paper.)

integrated from the coast to 300 km offshore, yielding the accumulated meridional transport. The LC transport is defined as the maximum accumulated poleward transport within 300 km from the coast. The LC transport tends to be weaker in austral summer (warm colours in Fig. 14) than in late austral autumn (cooler colours). The southward transport tends to decrease as the

Table 1
Best-fit linear curves and 95% confidence intervals in Fig. 14. T_{LC} is the southward Leeuwin Current transport (Sv), T_{CC} is the northward Capes Current transport (Sv), τ^y is the meridional wind stress ($\mathrm{N\,m^{-2}}$), and h_{1026} is the depth (m) of the 1026 $\mathrm{kg\,m^{-3}}$ isopycnal.

(a)	$T_{LC}=(-33.0\pm17.0)(\mathrm{Sv\,N^{-1}\,m^2})\tau^y+(7.4\pm1.9)(\mathrm{Sv})$
(b)	$T_{LC}=(0.07\pm0.07)(\mathrm{Sv\,m^{-1}})h_{1026}+(-14.16\pm17.52)(\mathrm{Sv})$
(c)	$T_{CC}=(3.2\pm1.0)(\mathrm{Sv\,N^{-1}\,m^2})\tau^y+(-0.2\pm0.1)(\mathrm{Sv})$
(d)	$T_{CC}=(-0.6\pm0.3)T_{LC}+(0.4\pm0.1)(\mathrm{Sv})$

meridional wind stress increases (Fig. 14). The anomalously large peak in LC transport corresponds to weak southerly winds (red + in Fig. 14a) and its value, ~9 Sv, is similar in magnitude to the monthly mean value reported in Feng et al. (2013). Hence weak southerly wind stress corresponds with the rapid increase in LC transport. Table 1 presents the best-fit linear curves and the 95% confidence intervals.

The LC transport is also linked to the remote wind forcing, where its southward transport appears to be correlated with the depth of the 1026 $\mathrm{kg\,m^{-3}}$ isopycnal in the northern part of the domain. We use an average depth from the northern part of the domain because Kelvin waves propagate this signal poleward into the boxed domain. The LC's transport is correlated with this depth, with deeper depths corresponding to greater poleward transports (Fig. 14b). Compared to the previous two years, 2011 has the deepest depth and greatest transports, including the marine heat wave peak time period (red +). In addition, a seasonal signal appears to be present, with shallower depths present in summer (warm colours) and deeper depths in autumn (cool colours). Thus, both weakened southerly winds and the remote wind forcing associated with the 2010–2011 La Niña contributed to the strong LC transports, which in turn led to anomalous warming during the marine heat wave.

Next, we investigate the changes in the near-shore Capes Current, where typical summertime advection of cooler water northward was suppressed in 2011 (Fig. 10b,e,h). The CC transport is calculated from the maximum northward accumulated transport from the coast to 100 m depth. If no northward flow is present (i.e. no CC), then the accumulated transport at 100 m depth is used. We focus only on the region from 32°S to 28°S. The CC transport tends to increase when the southerly wind stress is stronger (Fig. 14c). For 2009 and 2010, the mean CC transport tends to be greatest in summer (warm colours) and weakest, but still positive, in autumn (cool colours). In contrast, during the marine heat wave the meridional transport over the shelf is negative, i.e. southward (red +). This reversal of the northward CC transport is likely due to the anomalous weakening of the southerly wind stress. This reversal explains why the cooling associated with upwelling and northward advection is not present over the shelf (see ΔT_{ADV} in Fig. 10). Finally, Fig. 14d plots the Capes and Leeuwin Current transports against one another. This plot highlights that both boundary current transports were anomalous in February 2011, both in magnitude and in seasonal timing.

4. Summary and discussion

4.1. Sea surface temperature and velocity fields

In austral summer 2011, an extreme increase in sea surface temperature (SST) occurred offshore of Western Australia, an event known as the 2011 Ningaloo Niño. A regional ocean model is configured from 2009 through 2011 in order to analyse the mechanisms and forcings responsible for this shelf-scale warming. Off the west coast of Australia, the SST rapidly rises from January to March, followed by a slower decrease to April 30. We use the ocean model to investigate the processes that cause the spatial pattern of this warming. SST anomalies are associated with positive sea level anomalies and spread offshore from the coast. After the peak in SST, offshore propagation of eddies appears to contribute to offshore warming.

In 2011, the velocity field in the upper 250 m is more energetic with faster speeds than the previous two years. In February 2011, prior to the peak in warming, the LC has speeds greater than 0.35 $\mathrm{m\,s^{-1}}$ from Cape Leeuwin to Shark Bay, with speeds exceeding 0.5 $\mathrm{m\,s^{-1}}$ in some regions. The typical northward CC is suppressed, and poleward flow appears over the shelf. Instead of advecting cooler water northward, the shelf current advects warmer water poleward.

4.2. Temperature budget during the marine heat wave

In early 2011, the greatest warming occurred over the continental shelf and extended from Cape Leeuwin to the North West Cape. We use a temperature budget for the upper 60 m to determine the relative importance of advection and air–sea heat flux to the net change in temperature. For a significant region off the west coast, the warming is dominated by total advection. Near the coast, cooling associated with the northward flowing CC is damped. A volume budget is used to quantify the contributions from advection and air–sea heat flux to the net change in near-surface temperature. For 2009 and 2010, the change in temperature from January 1 to March 1 is controlled primarily by the total air–sea heat flux. During the 2011 marine heat wave, however, advection dominates the warming, causing ≈2/3 of the temperature change with air–sea heat fluxes contributing ≈1/3. After the warming peak, the temperature change decreases slowly, yielding the asymmetric peak seen in both the model SST and TMI SST. The temperature budget shows that this asymmetry is due to cooling by air–sea heat fluxes with little impact from advection.

4.3. Remote and local wind forcing impact on the coastal transports

During 2011, the Leeuwin Current's southward transport increased due to remote and local wind forcing. The intensified southward transport contributed to the shelf-scale warming prior to the peak of the marine heat wave. The depth of the 1026 $\mathrm{kg\,m^{-3}}$ isopycnal is used as a measure of the remote wind forcing, and greater depths correlate with a strengthened LC transport. This isopycnal depth was deeper nearly everywhere off the west coast in 2011, consistent with the large LC transports at the peak of the marine heat wave. In February 2011, local wind forcing appears to have had a significant impact on both the Leeuwin and Capes Current. Reduced southerly winds led to a stronger LC transport and a suppressed CC. The correlations between forcings and transports may guide predictions of advection's role in future marine heat waves off Western Australia. There are model prediction skills of the LC (Hendon and Wang, 2010) and the Ningaloo Niño (Doi et al., 2013), mostly based on the model skills to predict ENSO events. Further model improvement is necessary before the regional air–sea coupling can be well assimilated in climate models (Kataoka et al., 2013; Marshall et al., revised).

4.4. Model uncertainties

The model simulation supports the role of air–sea heat flux in contributing to the peak of the marine heat wave in the offshore region off Western Australia. Although all the reanalysis and forecast products exhibit positive heat flux anomalies into the ocean in the offshore region, there are discrepancies in the spatial

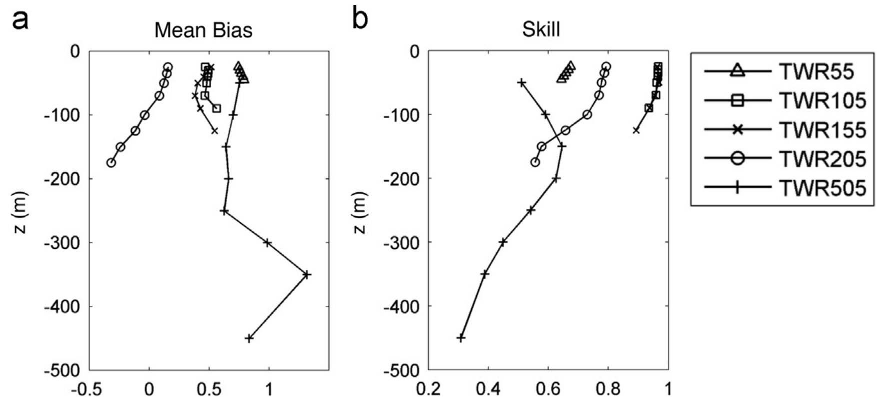

Fig. 15. Vertical profiles of model-data comparison for all Two Rocks transect moorings TWR55, TWR105, TWR155, TWR205, TWR505. The profiles show the model's (a) mean bias (°C) and (b) skill score, where the symbols corresponding to each mooring are shown in the right panel.

pattern of the heat flux anomalies, especially in the nearshore region. In the nearshore region, GODAS shows strong positive heat flux anomaly, while ECMWF and TROPFlux show weak positive heat flux anomaly (Feng et al., 2013).

The ACCESS-G Numerical Weather Prediction forecast, however, shows a negative heat flux anomaly in the LC and the nearshore region. Thus, in the ROMS model simulation, the LC advection is the dominant driver of the warming in the nearshore area. It is crucial to better quantify the heat flux in the nearshore region with a high resolution reanalysis. Higher nearshore resolution is needed to capture spatial patterns of the warming signals along the coast, which is important to predict the risks of coral bleaching and fish kills in future warming events.

Finally, another source of uncertainty is that the model's minimum depth is 30 m. In a model with shallower depths, a positive air–sea heat flux could lead to faster warming near the coast. Hence the warming may be underestimated near the coast owing to the depth limitation in the model. Continued long-term monitoring of the thermal structure in near-shore regions is important for understanding how these events impact ecosystems and coral growth (Zinke et al., 2014). In addition, long-term monitoring is important given that warming trends impact the magnitude of Ningaloo Niño events (Zinke et al., 2014).

4.5. Future work

Future work is necessary to test the contributions of total air–sea heat flux and advection to the warming event, given the uncertainty in heat flux products. In addition, a suite of numerical experiments could be performed to determine the relative roles of remote and local wind forcing to the strengthening of the LC. These experiments will allow a more in-depth analysis of how the LC intensified in early 2011 in response to each forcing. In addition, preliminary analysis from our model simulation indicates that a shelf-scale freshening occurred during the marine heat wave event. The LC intensification can cause an increased southward transport of fresh tropical water. Further research is underway to investigate the salinity anomalies during the 2011 Ninagloo Niño.

Acknowledgements

M. Feng and L. Zhong are supported by the CSIRO Wealth From Oceans Flagship, Australian Integrated Marine Observing System, and Fisheries Research and Development Corporation. This research is partly supported by the Australian Government Department of the Environment, the Bureau of Meteorology and CSIRO through the Australian Climate Change Science Programme. J. Benthuysen acknowledges support from the ARC Centre of Excellence for Climate System Science (CE110001028). J. Benthuysen and M. Feng acknowledge the support of ARC Discovery Project DP130102088. TMI data are produced by Remote Sensing Systems and sponsored by the NASA Earth Science MEaSUREs DISCOVER Project. We thank Jay McCreary, Eric Oliver, Tatiana Rykova, and two anonymous reviewers for reviews.

Appendix A

We use the mean bias and skill score to quantify the overall predictive skill of the ROMS model. The mean bias is

$$\textit{Mean Bias} = \langle m \rangle - \langle o \rangle, \tag{4}$$

where $\langle m \rangle$ and $\langle o \rangle$ are the respective mean values of the time series of model results and mooring observations. Fig. 15a plots the mean bias from the model. The model has warm bias at all five stations except at TWR205, where there is a cool bias at deep depths. The mean bias is around or less than 0.5 °C at TWR105, TWR155 and TWR205 moorings deployed in the intermediate water depth. At TWR55 and TWR505 in water depths of 55 m and 505 m respectively, the mean bias is about 0.75 °C but becomes larger toward deeper depths.

The skill score (Wilmott, 1981) has been used to evaluate ROMS performance (e.g. Warner et al., 2005) and is defined as

$$\textit{Skill} = 1 - \frac{\sum |X_{model} - X_{obs}|^2}{\sum \left(|X_{model} - \overline{X}_{obs}| + |X_{obs} - \overline{X}_{obs}| \right)^2}, \tag{5}$$

where X is the variable for comparison, $\overline{X}$ is the variable's time mean, and *model* and *obs* denote the model results and observations, respectively. A skill score of 1.0 occurs when the model results perfectly agree with observations and a skill score of 0 occurs when they completely disagree. Fig. 15b plots the skill score, and the model is most skillful at moorings TWR105 and TWR155 and is the least skillful at TWR505. The vertically averaged skill is as high as 0.96 and 0.95 at these two moorings, but decreases to 0.66, 0.71 and 0.51 at moorings TWR55, TWR205 and TWR505, respectively. These values are comparable to other skill scores (e.g. Li et al., 2005; Warner et al., 2005) in ROMS models.

References

Australian Bureau of Meteorology, 2010. Operational implementation of the ACCESS Numerical Weather Prediction systems. NMOC Operations Bulletin No. 83.
Benthuysen, J., Furue, R., McCreary, J.P., Bindoff, N.L., Phillips, H.E., 2014. Dynamics of the Leeuwin Current: Part 2. Impacts of mixing, friction, and advection on a

buoyancy-driven eastern boundary current over a shelf. Dyn. Atmos. Oceans 65, 39–63.
Bracco, A., Kucharski, F., Molteni, F., Hazeleger, W., Severijns, C., 2005. Internal and forced modes of variability in the Indian Ocean. Geophys. Res. Lett. 32, L12707. http://dx.doi.org/10.1029/2005GL023154.
Chapman, D.C., 1985. Numerical treatment of cross-shelf open boundaries in a barotropic coastal ocean model. J. Phys. Oceanogr. 15, 1060–1075.
Cresswell, G.R., Golding, T.J., 1980. Observations of a south-flowing current in the southeastern Indian Ocean. Deep Sea Res. 27A, 449–466.
Doi, T., Behera, S.K., Yamagata, T., 2013. Predictability of the Ningaloo Niño/Niña. Nat. Sci. Rep. 3, 2892, http://dx.doi.org/10.1038/srep02892.
Domingues, C.M., Wijffels, S.E., Maltrud, M.E., Church, J.A., Tomczak, M., 2006. Role of eddies in cooling the Leeuwin Current. Geophys. Res. Lett. 33, L05603. http://dx.doi.org/10.1029/2005GL025216.
Fang, F., Morrow, R., 2003. Evolution, movement and decay of warm-core Leeuwin Current eddies. Deep Sea Res. II 50, 2245–2261.
Feng, M., Majewski, L.J., Fandry, C.B., Waite, A.M., 2007. Characteristics of two counter-rotating eddies in the Leeuwin Current system off the Western Australian coast. Deep Sea Res. II 54, 961–980.
Feng, M., Biastoch, A., Böning, C., Caputi, N., Meyers, G., 2008. Seasonal and interannual variations of upper ocean heat balance off the west coast of Australia. J. Geophys. Res. 113, C12025. http://dx.doi.org/10.1029/2008JC004908.
Feng, M., McPhaden, M.J., Xie, S.P., Hafner, J., 2013. La Niña forces unprecedented Leeuwin Current warming in 2011. Nat. Sci. Rep. 3, 1277. http://dx.doi.org/10.1038/srep01277.
Feng, M., Meyers, G., Pearce, A., Wijffels, S., 2003. Annual and interannual variations of the Leeuwin Current. J. Geophys. Res., 3355. http://dx.doi.org/10.1029/2002JC001763.
Feng, M., Wijffels, S., Godfrey, S., Meyers, G., 2005. Do eddies play a role in the momentum balance of the Leeuwin Current? J. Phys. Oceanogr. 35, 964–975.
Flather, R.A., 1976. A tidal model of the northwest European continental shelf. Mem. Soc. R. Sci. Liege 10, 141–164.
Furue, R., McCreary, J.P., Benthuysen, J., Phillips, H.E., Bindoff, N.L., 2013. Dynamics of the Leeuwin Current: Part 1. Coastal flows in an inviscid, variable-density, layer model. Dyn. Atmos. Oceans 63, 24–59.
Hendon, H.H., Wang, G., 2010. Seasonal prediction of the Leeuwin Current using the POAMA dynamical seasonal forecast model. Clim. Dyn. 34, 1129–1137.
Kataoka, T., Tozuka, T., Behera, S., Yamagata, T., 2013. On the Ningaloo Niño/Niña. Clim. Dyn. 20, 1–20. http://dx.doi.org/10.1007/s00382-013-1961-z.
Large, W.G., McWilliams, J.C., Doney, S.C., 1994. Oceanic vertical mixing: A review and a model with a nonlocal boundary layer parameterization. Rev. Geophys. 32, 363–403. http://dx.doi.org/10.1029/94RG01872.
Li, M., Zhong, L., Boicourt, W.C., 2005. Simulations of Chesapeake Bay estuary: Sensitivity to turbulence mixing parameterizations and comparison with observations. J. Geophys. Res. 110, C12004. http://dx.doi.org/10.1029/2004JC002585.
Marchesiello, P., McWilliams, J.C., Shchepetkin, A., 2001. Open boundary conditions for long-term integration of regional oceanic models. Ocean Model. 3, 1–20.
Marchesiello, P., McWilliams, J.C., Shchepetkin, A., 2003. Equilibrium structure and dynamics of the California current system. J. Phys. Oceanogr. 33, 753–783.
Marshall, A.G., Hendon, H.H., Feng, M., Schiller, A. Initiation and amplification of the Ningaloo Niño. Clim. Dyn., revised.
Meuleners, M.J., Pattiaratchi, C.B., Ivey, G.N., 2007. Numerical modelling of the mean flow characteristics of the Leeuwin Current System. Deep Sea Res. II 54, 837–858.
Oke, P.R., Brassington, G.B., Griffin, D.A., Schiller, A., 2008. The Bluelink ocean data assimilation system (BODAS). Ocean Model. 21, 46–70.
Paterson, H.L., Feng, M., Waite, A.M., Gomis, D., Beckley, L.E., Holliday, D., Thompson, P.A., 2008. Physical and chemical signatures of a developing anticyclonic eddy in the Leeuwin Current, eastern Indian Ocean. J. Geophys. Res. 113, C07049. http://dx.doi.org/10.1029/2007JC004707.
Paulson, C.A., Simpson, J.J., 1977. Irradiance measurements in the upper ocean. J. Phys. Oceanogr. 7, 952–956.
Pearce, A., Pattiaratchi, C., 1999. The Capes Current: a summer countercurrent flowing past Cape Leeuwin and Cape Naturaliste, Western Australia. Cont. Shelf Res. 19, 401–420.
Pearce, A.F., Feng, M., 2013. The rise and fall of the "marine heat wave" off Western Australia during the summer of 2010/2011. J. Mar. Sci. 111–112, 139–156.
Rossi, V., Feng, M., Pattiaratchi, C., Roughan, M., Waite, A.M., 2013a. Linking synoptic forcing and local mesoscale processes with biological dynamics off Ningaloo Reef. J. Geophys. Res.: Oceans 118, 1211–1225. http://dx.doi.org/10.1002/jgrc.20110.
Rossi, V., Feng, M., Pattiaratchi, C., Roughan, M., Waite, A.M., 2013b. On the factors influencing the development of sporadic upwelling in the Leeuwin Current system. J. Geophys. Res.: Oceans 118, 3608–3621. http://dx.doi.org/10.1002/jgrc.20242.
Shchepetkin, A.F., McWilliams, J.C., 2005. The regional oceanic modeling system (ROMS): a split-explicit, free-surface, topography-following-coordinate oceanic model. Ocean Model. 9, 347–404.
Shinoda, T., Hendon, H.H., Alexander, M.A., 2004. Surface and subsurface dipole variability in the Indian Ocean and its relation with ENSO. Deep Sea Res. I 51, 619–635.
Sikiric, M., Janekovic, I., Kuzmic, M., 2009. A new approach to bathymetry smoothing in sigma-coordinate ocean models. Ocean Model. 29, 128–136.
Singh, P., Chowdary, J.S., Gnanaseelan, C., 2013. Impact of prolonged La Niña events on the Indian Ocean with a special emphasis on southwest Tropical Indian Ocean SST. Global Planet. Change 100, 28–37.
Warner, J.C., Geyer, W.R., Lerczak, J.A., 2005. Numerical modeling of an estuary: A comprehensive skill assessment. J. Geophys. Res. 110, C05001. http://dx.doi.org/10.1029/2004JC002691.
Weller, E., Holliday, D., Feng, M., Beckley, L., Thompson, P., 2011. A continental shelf scale examination of the Leeuwin Current off Western Australia during the austral autumn–winter. Cont. Shelf Res. 31, 1858–1868.
Wentz, F.J., 1997. A well-calibrated ocean algorithm for special sensor microwave/imager. J. Geophys. Res. 102, 8703–8718. http://dx.doi.org/10.1029/96JC01751.
Wernberg, T., Smale, D.A., Tuya, F., Thomsen, M.S., Langlois, T.J., de Bettignies, T., Bennett, S., Rousseaux, C.S., 2013. An extreme climatic event alters marine ecosystem structure in a global biodiversity hotspot. Nat. Clim. Change 3, doi: http://dx.doi.org/10.1038/nclimate1627.
Wilmott, C.J., 1981. On the validation of models. Phys. Geogr. 2, 184–194.
Woo, M., Pattiaratchi, C., Schroeder, W., 2006. Summer surface circulation along the Gascoyne continental shelf, Western Australia. Cont. Shelf Res. 26, 132–152.
Zinke, J., Rountrey, A., Feng, M., Xie, S.P., Dissard, D., Rankenburg, K., Lough, J.M., McCulloch, M.T., 2014. Corals record long-term Leeuwin current variability including Ningaloo Niño/Niña since 1795. Nat. Commun. 5, 3607. http://dx.doi.org/10.1038/ncomms4607.